NANO LETTERS

Letter

pubs.acs.org/NanoLett

TiO_2 Anatase with a Bandgap in the Visible Region

Christian Dette,[†] Miguel A. Pérez-Osorio,[‡] Christopher S. Kley,[†] Paul Punke,[†] Christopher E. Patrick,[‡] Peter Jacobson,[†] Feliciano Giustino,[‡] Soon Jung Jung,*[,†] and Klaus Kern[†,§]

[†]Max Planck Institute for Solid State Research, Heisenbergstrasse 1, 70569 Stuttgart, Germany

[‡]Department of Materials, University of Oxford, Parks Road, Oxford OX1 3PH, United Kingdom

[§]Institute de Physique de la Matière Condensée, École Polytechnique Fédérale de Lausanne, 1015 Lausanne, Switzerland

Supporting Information

ABSTRACT: TiO_2 anatase plays a central role in energy and environmental research. A major bottleneck toward developing artificial photosynthesis with TiO_2 is that it only absorbs ultraviolet light, owing to its large bandgap of 3.2 eV. If one could reduce the bandgap of anatase to the visible region, TiO_2-based photocatalysis could become a competitive clean energy source. Here, using scanning tunneling microscopy and spectroscopy in conjunction with density functional theory calculations, we report the discovery of a highly reactive titanium-terminated anatase surface with a reduced bandgap of less than 2 eV, stretching into the red portion of the solar spectrum. By tuning the surface preparation conditions, we can reversibly switch between the standard anatase surface and the newly discovered low bandgap surface phase. The identification of a TiO_2 anatase surface phase with a bandgap in the visible and high chemical reactivity has important implications for solar energy conversion, photocatalysis, and artificial photosynthesis.

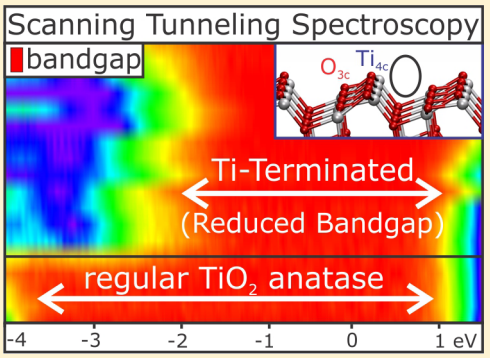

KEYWORDS: *Photocatalysis, TiO_2 anatase, titanium-terminated surface phase, bandgap reduction to the visible, scanning tunneling microscopy and spectroscopy, density functional theory*

Anatase is the technologically most relevant polymorph of titanium dioxide, finding applications in dye-sensitized solar cells,[1,2] lithium ion batteries,[3,4] as a catalyst,[5,6] and in self-cleaning coatings.[7] The relative lack of studies on well-defined anatase surfaces, compared to the archetypal rutile TiO_2, is due to the challenging growth of large synthetic crystals and the scarcity of high quality natural mineral single crystals. While rutile and anatase are both constructed from octahedral building blocks, differences in the octahedral arrangement and distortion between rutile and anatase result in distinct behavior for each polymorph. In particular, anatase efficiently separates photoexcited charge carriers which is key to the superior performance of anatase over rutile in photocatalytic applications.[8−10]

The drawback to using anatase in photocatalytic applications lies in its large bandgap (3.2 eV), which limits the spectrum of photons that can create electron−hole pairs to participate in oxidation or reduction reactions to the UV and corresponds to only 4% of the incident solar energy. Hence, reducing the bandgap of TiO_2 to coincide with the visible spectrum is a highly active area of research with strategies based on doping, ion implantation, metal loading, and composite semiconductors.[11−17] However, in most cases the photocatalytic efficiency suffers from defect-induced recombination losses and a limited solubility of substitutional heteroatoms.[18] Another approach is the introduction of bandgap states by a modification of the surface as reported on rutile (001)[19] and (011).[20,21]

Considerable effort has been expended to increase the reactivity of pristine TiO_2 anatase by controlling the dominant crystal facet[22] or by introducing oxygen vacancies.[23] In the broadest sense, oxygen vacancies in TiO_2 are preferential active sites for molecular adsorption and dissociation, in addition to being traps for photoexcited charged carriers.[5] However, isolated oxygen vacancies at the energetically most favorable anatase (101) surface are not stable and diffuse to subsurface layers, in contrast to TiO_2 rutile (110). In addition, isolated oxygen vacancies have been shown to exhibit repulsive interactions.[24−26] The tendency for single oxygen vacancies to diffuse away from this catalytically active surface is detrimental to the overall reactivity of anatase (101). These qualities suggest that there are limits to the chemical reactivity of the anatase (101) surface through the creation of isolated oxygen vacancies.

In this article, we introduce a new surface phase of anatase (101), which combines two highly desirable attributes, namely a reduced bandgap in the visible and higher chemical reactivity. This surface phase lacks the outermost oxygen layer of the stoichiometric surface and is fully covered by a layer of Ti_{4c} atoms. By simply controlling the oxidation time and temperature, we can reversibly switch the surface termination between

Received: August 14, 2014
Revised: September 18, 2014
Published: September 24, 2014

   dx.doi.org/10.1021/nl503131s | *Nano Lett.* 2014, 14, 6533−6538

an oxygen-terminated stoichiometric phase and a titanium-terminated nonstoichiometric phase. The electronic structure at different atomic positions, e.g., step edges and terraces of the new surface termination, was directly measured by low-temperature scanning tunneling microscopy and spectroscopy (STM/STS) and compared with the oxygen-terminated phase. Comparing our STM/STS data with first-principles calculations based on density functional theory (DFT), we demonstrate that the new phase is a substoichiometric, titanium-terminated anatase surface. We are able to establish that the reduced bandgap originates from the presence of surface gap states associated with the exposed Ti_{4c} and Ti_{5c} sites. This unprecedented titanium-terminated surface, with a bandgap in the visible region, holds promise for improving the harvesting of photons in a broader range of the solar spectrum, resulting in enhanced heterogeneous catalysis, photovoltaics, and other industrial applications.

The stoichiometric oxygen-terminated surface (Figure 1a,b) was prepared by a combination of sputtering, annealing, and oxygen-annealing (detailed procedures in Methods). By increasing the temperature of the oxygen annealing from 670 to 920 K, a titanium-terminated anatase surface phase is created on the stoichiometric oxygen-terminated surface (Figure 1d,e), which is overlaid with a blue color to discriminate it more clearly from the oxygen-terminated surface in red (original data in Supplementary Figure S1). Three observations are immediately apparent from this STM topograph: the titanium-terminated surface shows a different electronic contrast to the oxygen-terminated surface, the titanium-terminated regions reveal a high density of adsorbates, while the oxygen-terminated regions are free of adsorbates and bulk defects, and terraces of the titanium-terminated surface have a different step edge configuration. The oxygen-terminated surface (Figure 1a,b) shows characteristic trapezoidal terraces with step edges oriented along the [010], [11−1], and [−111] directions.[18] The [010] edge is adsorbate free, while the [−111] edge is often partially covered with adsorbates after standard cleaning procedures indicating that the reactivity of [−111] oriented edges is higher than that of [010] oriented edges and the terrace, which well agrees with previous reports.[27] Removing the outermost layer of bridging oxygen atoms results in a new preferential step direction with step edges oriented in the [010], [12−1], and [−111] directions, which can be seen in Figure 1e. These [12−1] steps are only found on the titanium-terminated phase (Supplementary Figure S2, ball-and-stick model Figure S9) and indicate a change in the local bonding environment of the surface titanium atoms. In addition, STM linescans show that the terrace of the Ti-terminated phase has a step height of 3 Å and, thus, is an intermediate step terrace structure compared to steps on the O-terminated phase which have a height of 4.5 Å (Supplementary Figure S3).

Terraces with an oxygen-termination show a uniform contrast indicating a high degree of homogeneity and possess few reactive oxygen vacancy sites (surface or subsurface) indicative of a sample that is not heavily bulk reduced.[28] The titanium-terminated surface phase can locally cover more than 50% of the surface and can be annealed up to 500 °C for 30 min without reverting to the stoichiometric surface (Figure 1d). Moreover, the oxygen-terminated phase can be fully recovered when the crystal is further annealed in oxygen atmosphere at 920 K. Alternating these surface preparation procedures allows the controlled switching of a purely oxygen-terminated surface to a partially covered titanium-terminated surface, and vice versa.

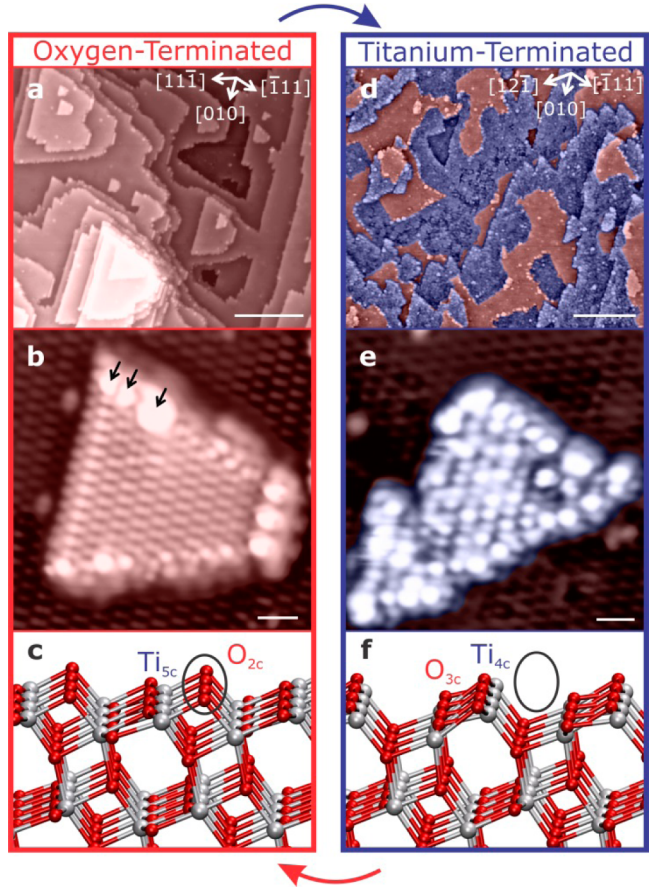

Figure 1. Reversible transition of the TiO_2 anatase (101) surface phases. (a) STM image (V_s = 2.0 V, I = 0.1 nA, T = 5 K) shows the clean oxygen-terminated anatase (101) surface. The preferential orientations of step edges are indicated by white arrows. (b) High−resolution STM image of the anatase (101) surface with trapezoidal island along the [010], [−111], and [11−1] direction. The black arrows indicate adsorbates that sit on the [−111] step edge. (d) STM image of a titanium-terminated surface (blue overlay) coexisting with an oxygen-terminated surface (red overlay) on the same crystal, following a modified preparation method (see SI for more details). The preferential orientation of the Ti-terminated step edges are changed to [010], [−111], and [12−1]. (e) High-resolution STM image of a Ti-terminated island. The oxygen-terminated surface (shown in a and b) can be recovered by additional annealing in oxygen atmosphere. (c, f) Ball-and-stick models of the optimized structures of the oxygen- and titanium-terminated anatase (101) surface. The structural model of the titanium-terminated (101) surface (f) is obtained by removing the bridging oxygen atoms (O_{2c}) from the oxygen-terminated surface, leading to the formation of Ti_{4c} atoms at the top of the surface and Ti_{5c} atoms underneath (scale bars: (a) and (d) 20 nm, (b) and (e) 1 nm).

The proposed and calculated structure of the Ti-terminated anatase surface phase is shown in Figure 1f, together with the conventional O-terminated surface phase in Figure 1c. Upon removing the topmost oxygen atoms from the pristine anatase (101) surface (circled area), the structure undergoes relaxation, with the 3-fold coordinated oxygen atoms (O_{3c}) relaxing outward by 0.3 Å. Additionally, while on the pristine (101) surface the bright protrusions observed in STM topographs originate from the 5-fold coordinated Ti atoms (Ti_{5c}), on the

dx.doi.org/10.1021/nl503131s | Nano Lett. 2014, 14, 6533−6538

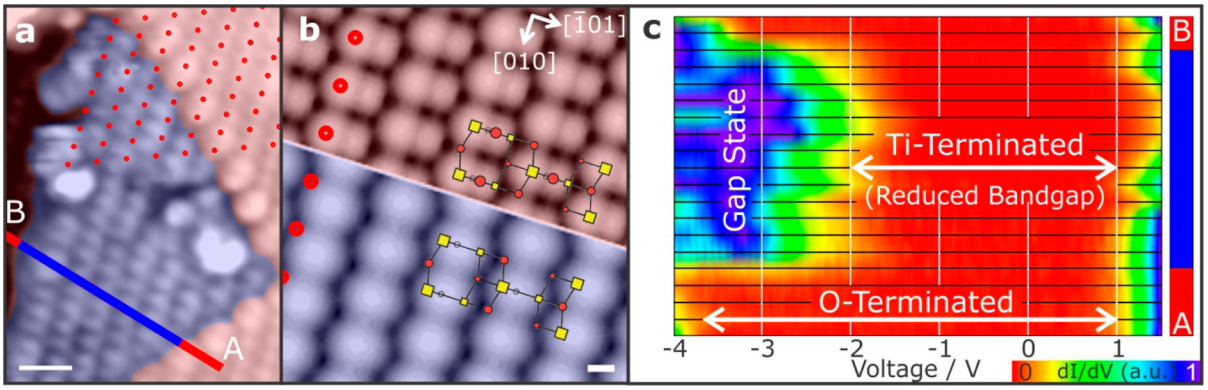

Figure 2. Electronic structure and topography of the Ti-terminated surface of TiO_2 anatase (101). (a) Atomic resolution STM image (V_s = 2.0 V, I = 0.1 nA) reveals a Ti-terminated patch (blue) embedded in an oxygen-terminated terrace (red). (b) DFT-calculated STM images of the oxygen- and titanium-terminated (101) surfaces for a positive bias voltage of 1 eV. The overlaid models indicate the atomic positions of the Ti (yellow rectangles) and O (red circles) atoms on the surface. The red dotted lines in (a) and (b) highlight the offset of the bright protrusions between the two different phases. (c) Top view of a waterfall plot of tunneling spectra taken on the line in (a). The variance in the CBM is an artifact due to the normalization of the differential conductance to 1 (see Supplementary Figure S4). The spectra recorded at the O-terminated surface (red lines) reveal the common featureless bandgap of ∼4 eV. The spectra on the blue line which are taken on the Ti-termination show a reduced bandgap (2 eV) due to the bandgap state at −3.3 V (scalebars: (a) 1 nm, (b) 2 Å).

reduced surface the bright protrusions arise from the newly formed Ti_{4c} atoms and the Ti_{5c} atoms underneath.

Figure 2a shows a close-up of a titanium-terminated patch embedded in an oxygen-terminated terrace. Notably, a clear shift of the bright protrusions between the titanium- and oxygen-terminated surface phases is revealed. The red dots mark the center of the bright protrusion. Extending the regular lattice from the oxygen-terminated surface to the titanium-terminated surface, the red overlay clearly sits between the rows on the titanium-terminated surface. DFT calculations were performed to generate simulated STM topographs of the different surface phases and are shown in Figure 2b. The features observed in the experimental images are well-reproduced by our calculations and can be rationalized as follows: Upon reduction of the pristine surface, adjacent rows of Ti_{5c} and Ti_{6c} atoms are replaced by corresponding rows of Ti_{4c} and Ti_{5c} atoms (Figure 2b). The modified oxidation state of these atoms and the additional contribution of the newly formed rows of Ti_{5c} lead to a rounding of the protrusions and an offset of the topograph. The shape of the protrusions is slightly dependent on the choice of the Hubbard parameter in the calculations, but the offset between rows is largely independent of the calculation details.

High-resolution STM imaging combined with atomically resolved spectroscopy was used to carefully examine the electronic structure of the Ti-terminated surface as shown in Figure 2. We have mapped the local density of states in an atom-specific manner over both the oxygen- and titanium-terminated surfaces. A set of I−V curves is plotted for 20 positions on a line traversing the two surface phases (Figure 2a) and is depicted in a top view of a normalized waterfall plot in Figure 2c. The red regions of the waterfall plot correspond to negligible differential conductance and indicate the bandgap region. Spectra taken on the red lines are taken on the oxygen-terminated surface and show the onset of the valence band maximum (VBM) and conduction band minimum (CBM) separated by a bandgap of 4 eV − an overestimation due to tip-induced band bending common for semiconductors[29,30] (CBM 0.5 V, VBM −3.5 V). Spectra obtained on the blue line reveal a drastically reduced bandgap of 2 eV (CBM 0.5 V, VBM −1.5 V) with an additional peak at −3.3 V. Comparing our results to the values of previous reports,[19,20] the reduction of the bandgap on the Ti-terminated surface is significantly larger (details see SI). Our DFT calculations indicate that this additional peak arises from occupied d states of the undercoordinated Ti_{4c} and Ti_{5c} atoms at the surface, as suggested in refs 31−35. The electron spins of these atoms are arranged in a paramagnetic ground state, with a magnetization of 1.0 Bohr magneton per surface Ti atom; i.e., we find one unpaired electron per Ti atom as expected. For clarity, the calculations described here correspond to a ferromagnetic alignment, with other configurations yielding similar results. The existence of gap states corresponding to O vacancies and the creation of Ti^{3+} species is well-established in bulk TiO_2 polymorphs.[36,37] However, at variance with the standard defects in bulk oxides, in the present case the gap states define completely delocalized surface states. The presence of occupied gap states reduces the bandgap of the Ti-terminated surface by raising the valence band maximum by 1−1.5 eV with respect to the pristine surface. For this calculation the Hubbard parameter was set to 3.5 eV, corresponding to the average of those previously used to describe O vacancies in bulk TiO_2,[38−40] and very close to that determined using self-consistent linear-response theory, 3.3 eV.[38]

Combining atomically resolved spectroscopy with DFT calculations we now turn our focus to the atomic and electronic structure of step edges on the oxygen-terminated surface. Our principal observation is that [−111] step edges are not stoichiometric and contain oxygen vacancies. The presence of oxygen vacancies (and undercoordinated Ti sites) leads in turn to a bandgap state identical to that observed on the titanium-terminated surface. For the oxygen-termination, step edges along the [010] direction exhibit dim features (Figure 3a) in between the bright protrusions. To understand the origin of these features we simulated STM images of these step edges from first-principles utilizing the atomistic models, which correspond to those analyzed in ref 41. Our calculated STM image of the stoichiometric [010] step edge is in close agreement with experiment (Figure 3b). Considering the atomistic model of this step edge in Figure 3c, we assign the dim features to rows of Ti_{5c} atoms at the edge. For step edges along the [−111] direction, our calculations were able to

dx.doi.org/10.1021/nl503131s | Nano Lett. 2014, 14, 6533−6538

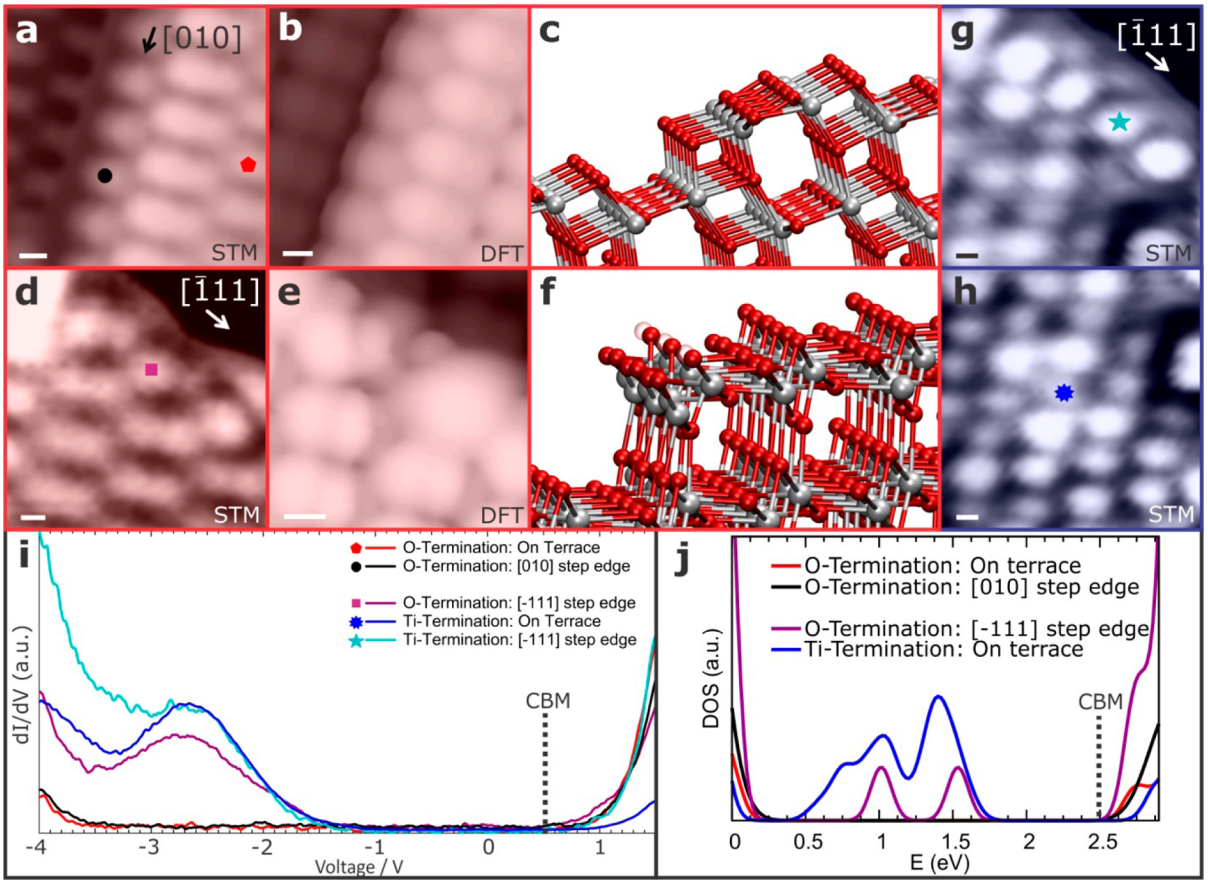

Figure 3. Comparison of electronic structure of the O-terminated and Ti-terminated surfaces. (a, d) Magnified STM image (V_s = 2.0 V, I = 0.1 nA) of the step edges oriented along the [010] and [−111] directions of the oxygen-terminated island in Figure 1b. (b, e) DFT-derived STM images and (c, f), optimized ball-and-stick models of the step edges imaged in (a) and (d), respectively. The atomistic model proposed for the step edge (d) is decorated with oxygen vacancies (one vacancy every two Ti atoms in the top row), indicated as hollowed spheres in (f). Additional views of this step edge are provided in Supplementary Figure S5. (g, h) Zoomed-in STM images of step edges and terrace of the titanium-terminated island in Figure 1d. (i) Representative tunneling spectra taken at different positions of the different surface phases. (j) DFT STS spectra of the step edges and surfaces of TiO_2 anatase. The CBM is depicted to relate the energies of the experimental and calculated spectroscopy data (scalebars = 2 Å).

reproduce the isolated protrusion at the edge of the measured topograph (purple square in Figure 3d) only after incorporating O vacancies, as shown in Figure 3e and f. Therefore, the [−111] step edge is decorated by O vacancies.

To clarify this aspect we turn to the STS analysis shown in Figure 3i and j. The red spectrum in Figure 3i is taken at the clean oxygen-terminated terrace, and the black spectrum was obtained at the unreactive [010] edge. Both spectra show the same behavior without any features between the VBM and CBM onsets. The purple spectrum obtained on the highly reactive [−111] edge shows a reduced bandgap of 2 V (CBM 0.5 V, VBM −1.5 V) with an additional peak around −2.7 V. This spectrum coincides with the spectra obtained at the titanium-terminated island (blue and teal). Therefore, we conclude that the titanium-terminated surface phase and the [−111] edge of the O-terminated surface have the same undercoordinated Ti_{4c} atoms due to missing oxygen atoms which lead to the bandgap reduction. Note that similar measurements were repeated at hundreds of different positions on different islands of the particular surface termination, thus proving the reproducibility. In line with our experimental observations, the calculated projected density of states of the stoichiometric [010] step edge on the pristine anatase (101) surface does not exhibit gap states. This observation applies more generally to all the atomistic models of stoichiometric step edges that we investigated.

For the [−111] edge, our calculations shown in Figure 3j indicate that the new feature in the bandgap appears only when we consider a nonstoichiometric step edge, as was done in Figure 3f. By analyzing the partial density of states, we find that this new peak is derived from the Ti 3d states of the Ti_{4c} atoms and leads to a reduction of the bandgap by approximately 1−1.5 eV. Considering the overestimation by tunneling spectroscopy and the typical underestimation by DFT-based calculations[42] of the bandgap, the calculated spectra are in good qualitative agreement with the experiment (Supplementary Figure S7). These observations strongly support the assignment of the [−111] topographs and STS data to an oxygen deficient step edge. Although the precise energetics of the gap states is sensitive to the choice of the Hubbard parameter, the qualitative features are robust, as we confirmed with separate calculations using the PBE0 functional.[43] The double-peak structure in Figure 3j was also reported in previous theoretical studies of O vacancies in bulk TiO_2[37] and is not resolved in the experiment.

Taken together, our combined experimental and theoretical analyses reveal a substoichiometric, titanium-terminated anatase (101) surface. This titanium-terminated surface represents a unique surface phase and cannot be considered as a simple

dx.doi.org/10.1021/nl503131s | Nano Lett. 2014, 14, 6533−6538

reduced anatase surface with isolated (subsurface) oxygen vacancies. Moreover, the undercoordinated Ti_{4c} atoms coalesce into entire domains with a high degree of structural similarity and a new electronic structure. The new proposed structure of the reactive [−111] step edge similar to the Ti-terminated surface gives an explanation for the increased reactivity. The titanium-terminated surface presented here augments the versatility of the technologically most important metal oxide, anatase TiO_2. The combination of a reduced surface bandgap and enhanced reactivity of undercoordinated Ti sites opens new possibilities in photovoltaics and photocatalytic applications.

Methods. *Sample Preparation.* We employed a naturally grown TiO_2 anatase (101) crystal which was polished, with a roughness of less than one lattice constant (SurfaceNet GmbH, Germany). The size of the crystal was $4 \times 4 \times 2$ mm^3 with a metallic opaque color. We prepared the crystal in situ in our preparation chamber (base pressure in the low 10^{-10} mbar) by repeated cycles of annealing (920 K, 10−30 min), Ar^+-sputtering (1 keV, 10 min) and annealing in oxygen atmosphere (670 K, 30−60 min, 1×10^{-6} mbar). The temperature ramp for heating was 2 K/s, while the speed for cooling was slower at 0.5 K/s.

Titanium-Terminated Surface Preparation. The anatase crystal was heated up to 920 K and remained at the temperature for 20 min with a maximum pressure of 2.0×10^{-9} mbar. Sputtering was performed at substrate temperatures below 330 K with an Ar-ion sputtering gun at energies of 1 keV for 10 min at a pressure of about 6×10^{-6} mbar, which resulted in a sample current of 1.1 μA. Sputtering was performed at grazing incidence, 20° to the surface plane. This annealing and sputtering cycle was repeated one more time. Afterward, the sample was annealed to 920 K for 10 min in ultrahigh vacuum. The chamber was backfilled with oxygen ($p = 8 \times 10^{-7}$ mbar) for 30 min while keeping the substrate at 920 K. Subsequently, the sample was annealed in vacuum for another 20 min at 920 K. Due to residual oxygen in the chamber during the post annealing step, the pressure decreased during this time from 6×10^{-9} mbar to 3.5×10^{-9} mbar. The crystal was cooled down slowly until it reached room temperature and then transferred into the STM operated at 5 K.

Oxygen-Terminated Surface Preparation. To recover the stoichiometric oxygen-terminated surface, the sample was annealed to 920 K. After 10 min of annealing in ultrahigh vacuum, the chamber was backfilled with oxygen until 8×10^{-7} mbar and the sample remained at the elevated temperature for 30 min. Afterward, the oxygen was pumped out, and the sample was post-annealed for 20 min. The pressure again decreased from 6×10^{-9} mbar to 3.5×10^{-9} mbar.

Measurements. We performed the experiments on the TiO_2 anatase (101) surface in a home-built 5K scanning tunneling microscope (STM) in constant current mode. The STM was equipped with electrochemical etched Pt−Ir tips bought from Agilent Technologies (N9801A), USA. Unless otherwise stated the set point current and voltage for the topography images was 100 pA and +2 V which means that the empty states were measured. The differential conductance measurements were performed with a set point current and bias of 100 pA and +1.5 V, respectively. The lock-in amplifier modulated the bias at a frequency of 2.5 kHz above the cutoff frequency of the feedback loop with a modulation voltage of 20 mV.

Computational Details. Density functional theory calculations were performed using the Perdew−Burke−Ernzerhof exchange and correlation functional,[44] as implemented in the Quantum ESPRESSO software package.[45] Only valence electrons were explicitly described, including the Ti 3s and 3p semicore states, and the core−valence interaction was taken into account by means of ultrasoft pseudopotentials.[46] The wave functions and charge density were represented through plane-wave basis sets with energy cutoffs of 35 and 200 Ry, respectively. Spin polarization was taken into account in the calculations of the Ti-terminated surface. In order to properly describe the energetics of the Ti 3d states we included Hubbard-like corrections by means of the simplified rotational-invariant formulation of ref 47. The calculated STM topographs and STS spectra reported in the manuscript were obtained using a value of the Hubbard parameter U of 3.5 eV. This value represents an average of the range of Hubbard parameters previously used to study O vacancies in bulk TiO_2,[38−40] and is close to the Hubbard parameter determined from first-principles using linear-response calculations.[38] Surface Brillouin zone integrations were carried out using 2×3 and 4×4 Monkhorst−Pack meshes, for the calculations of the step edges and of the extended surfaces, respectively. All structures were optimized within DFT+U using both conjugate-gradient and damped Car−Parrinello minimizations, until the forces on atoms were less than 0.04 eV/Å. The STM images were calculated within the Tersoff−Hamann approximation at constant current,[48] by considering electronic states within 1 eV from the conduction band edge. We note that for the pristine surface we find that the brightest protrusions correspond to Ti_{5c} atoms, while in ref 41 they were assigned to O_{2c}. Our test calculations indicate that this assignment is sensitive to small changes in atomistic and electronic structure for different values of the Hubbard U. The STS spectra were calculated as local density of states integrated over the terraces or the step edges.

■ ASSOCIATED CONTENT

Supporting Information

Calculation of the thermodynamic phase diagram, uncolored and unprocessed data, step edge orientation, step height measurement, additional structural models, thermodynamic stability graph, PBE0 DOS calculation, and onset calculation. This material is available free of charge via the Internet at http://pubs.acs.org.

■ AUTHOR INFORMATION

Corresponding Author

*E-mail: s.jung@fkf.mpg.de, phone: 0049-711-689-5249.

Notes

The authors declare no competing financial interest.

■ ACKNOWLEDGMENTS

P.J. acknowledges support from the Alexander von Humboldt Foundation. M.A.P.O., C.E.P., and F.G. were supported by the European Research Council (EU FP7/ERC grant no. 239578), the UK Engineering and Physical Sciences Research Council (grant no. EP/J009857/1), and the Leverhulme Trust (grant no. RL-2012-001). The calculations were performed at the Oxford Supercomputing Centre and at the Oxford Materials Modelling Laboratory. All structural models were rendered using VMD.[49]

■ ABBREVIATIONS

STM, scanning tunneling microscopy; STS, scanning tunneling spectroscopy; DFT, density functional theory; DOS, density of states; CBM, conduction band minimum; VBM, valence band minimum

■ REFERENCES

(1) Grätzel, M. *Inorg. Chem.* **2005**, *44*, 6841−6851.
(2) O'Regan, B.; Gratzel, M. *Nature* **1991**, *353*, 737−740.
(3) Wagemaker, M.; Kentgens, A. P. M.; Mulder, F. M. *Nature* **2002**, *418*, 397−399.
(4) Chen, J. S.; Tan, Y. L.; Li, C. M.; Cheah, Y. L.; Luan, D.; Madhavi, S.; Boey, F. Y. C.; Archer, L. A.; Lou, X. W. *J. Am. Chem. Soc.* **2010**, *132*, 6124−6130.
(5) Linsebigler, A. L.; Lu, G.; Yates, J. T. *Chem. Rev.* **1995**, *95*, 735−758.
(6) Fujishima, A.; Honda, K. *Nature* **1972**, *238*, 37−38.
(7) Wang, R.; Hashimoto, K.; Fujishima, A.; Chikuni, M.; Kojima, E.; Kitamura, A.; Shimohigoshi, M.; Watanabe, T. *Nature* **1997**, *388*, 431−432.
(8) Xu, M.; Gao, Y.; Moreno, E. M.; Kunst, M.; Muhler, M.; Wang, Y.; Idriss, H.; Wöll, C. *Phys. Rev. Lett.* **2011**, *106*, 138302 1−4.
(9) Stevanovic, A.; Büttner, M.; Zhang, Z.; Yates, J. T. *J. Am. Chem. Soc.* **2011**, *134*, 324−332.
(10) Stevanovic, A.; Yates, J. T. *J. Phys. Chem. C* **2013**, *117*, 24189−24195.
(11) Asahi, R.; Morikawa, T.; Ohwaki, T.; Aoki, K.; Taga, Y. *Science* **2001**, *293*, 269−271.
(12) Choi, W.; Termin, A.; Hoffmann, M. R. *J. Phys. Chem.* **1994**, *98*, 13669−13679.
(13) Ohsawa, T.; Lyubinetsky, I.; Du, Y.; Henderson, M. A.; Shutthanandan, V.; Chambers, S. A. *Phys. Rev. B* **2009**, *79*, 085401-1−7.
(14) Di Valentin, C.; Diebold, U.; Selloni, A. *Chem. Phys.* **2007**, *339*, vii−viii.
(15) Diwald, O.; Thompson, T. L.; Goralski, E. G.; Walck, S. D.; Yates, J. T. *J. Phys. Chem. B* **2003**, *108*, 52−57.
(16) Subramanian, V.; Wolf, E. E.; Kamat, P. V. *J. Am. Chem. Soc.* **2004**, *126*, 4943−4950.
(17) Robel, I.; Subramanian, V.; Kuno, M.; Kamat, P. V. *J. Am. Chem. Soc.* **2006**, *128*, 2385−2393.
(18) Diebold, U. *Surf. Sci. Rep.* **2003**, *48*, 53−229.
(19) Ariga, H.; Taniike, T.; Morikawa, H.; Tada, M.; Min, B. K.; Watanabe, K.; Matsumoto, Y.; Ikeda, S.; Saiki, K.; Iwasawa, Y. *J. Am. Chem. Soc.* **2009**, *131*, 14670−14672.
(20) Tao, J.; Luttrell, T.; Batzill, M. *Nat. Chem.* **2011**, *3*, 296−300.
(21) Liu, L.; Chen, X. *Chem. Rev.* **2014**, DOI: 10.1021/cr400624r.
(22) Yang, H. G.; Sun, C. H.; Qiao, S. Z.; Zou, J.; Liu, G.; Smith, S. C.; Cheng, H. M.; Lu, G. Q. *Nature* **2008**, *453*, 638−641.
(23) Wang, Y.; Sun, H.; Tan, S.; Feng, H.; Cheng, Z.; Zhao, J.; Zhao, A.; Wang, B.; Luo, Y.; Yang, J.; Hou, J. G. *Nat. Commun.* **2013**, *4* (2214), 1−8.
(24) Setvín, M.; Aschauer, U.; Scheiber, P.; Li, Y.-F.; Hou, W.; Schmid, M.; Selloni, A.; Diebold, U. *Science* **2013**, *341*, 988−991.
(25) Cheng, H.; Selloni, A. *Phys. Rev. B* **2009**, *79*, 0921011−4.
(26) Scheiber, P.; Fidler, M.; Dulub, O.; Schmid, M.; Diebold, U.; Hou, W.; Aschauer, U.; Selloni, A. *Phys. Rev. Lett.* **2012**, *109*, 136103 1−5.
(27) Setvin, M.; Hao, X.; Daniel, B.; Pavelec, J.; Novotny, Z.; Parkinson, G. S.; Schmid, M.; Kresse, G.; Franchini, C.; Diebold, U. *Angew. Chem., Int. Ed.* **2014**, *53*, 4714−4716.
(28) He, Y.; Dulub, O.; Cheng, H.; Selloni, A.; Diebold, U. *Phys. Rev. Lett.* **2009**, *102*, 106105 1−4.
(29) Feenstra, R. M.; Stroscio, J. A. *J. Vac. Sci. Technol., B* **1987**, *5*, 923−929.
(30) Kley, C. S.; Dette, C.; Rinke, G.; Patrick, C. E.; Čechal, J.; Jung, S. J.; Baur, M.; Dürr, M.; Rauschenbach, S.; Giustino, F.; Stepanow, S.; Kern, K. *Nano Lett.* **2014**, *14*, 563−569.
(31) Wendt, S.; Sprunger, P. T.; Lira, E.; Madsen, G. K. H.; Li, Z.; Hansen, J. Ø.; Matthiesen, J.; Blekinge-Rasmussen, A.; Lægsgaard, E.; Hammer, B.; Besenbacher, F. *Science* **2008**, *320*, 1755−1759.
(32) Papageorgiou, A. C.; Beglitis, N. S.; Pang, C. L.; Teobaldi, G.; Cabailh, G.; Chen, Q.; Fisher, A. J.; Hofer, W. A.; Thornton, G. *Proc. Natl. Acad. Sci. U.S.A.* **2010**, *107*, 2391−2396.
(33) Ganduglia-Pirovano, M. V.; Hofmann, A.; Sauer, J. *Surf. Sci. Rep.* **2007**, *62*, 219−270.
(34) Di Valentin, C.; Pacchioni, G.; Selloni, A. *Phys. Rev. Lett.* **2006**, *97*, 166803 1−4.
(35) Krischok, S.; Gunster, J.; Goodman, D. W.; Hofft, O.; Kempter, V. *Surf. Interface Anal.* **2005**, *37*, 77−82.
(36) Finazzi, E.; Di Valentin, C.; Pacchioni, G.; Selloni, A. *J. Chem. Phys.* **2008**, *129* (154113), 1−9.
(37) Di Valentin, C.; Pacchioni, G.; Selloni, A. *J. Phys. Chem. C* **2009**, *113*, 20543−20552.
(38) Mattioli, G.; Filippone, F.; Alippi, P.; Amore Bonapasta, A. *Phys. Rev. B* **2008**, *78*, 2412011−4.
(39) Morgan, B. J.; Watson, G. W. *Surf. Sci.* **2007**, *601*, 5034−5041.
(40) Cheng, H.; Selloni, A. *J. Chem. Phys.* **2009**, *131*, 054703 1−10.
(41) Gong, X.-Q.; Selloni, A.; Batzill, M.; Diebold, U. *Nat. Mater.* **2006**, *5*, 665−670.
(42) van Schilfgaarde, M.; Kotani, T.; Faleev, S. *Phys. Rev. Lett.* **2006**, *96*, 226402 1−4.
(43) Adamo, C.; Barone, V. *J. Chem. Phys.* **1999**, *110*, 6158−6170.
(44) Perdew, J. P.; Burke, K.; Ernzerhof, M. *Phys. Rev. Lett.* **1996**, *77*, 3865−3868.
(45) Giannozzi, P.; Stefano, B.; Nicola, B.; Matteo, C.; Roberto, C.; Carlo, C.; Davide, C.; Guido, L. C.; Matteo, C.; Ismaila, D.; Andrea Dal, C.; Stefano de, G.; Stefano, F.; Guido, F.; Ralph, G.; Uwe, G.; Christos, G.; Anton, K.; Michele, L.; Layla, M.-S.; Nicola, M.; Francesco, M.; Riccardo, M.; Stefano, P.; Alfredo, P.; Lorenzo, P.; Carlo, S.; Sandro, S.; Gabriele, S.; Ari, P. S.; Alexander, S.; Paolo, U.; Renata, M. W. *J. Phys.: Condens. Matter* **2009**, *21*, 395502 1−19.
(46) Vanderbilt, D. *Phys. Rev. B* **1990**, *41*, 7892−7895.
(47) Cococcioni, M.; de Gironcoli, S. *Phys. Rev. B* **2005**, *71*, 0351051−16.
(48) Tersoff, J.; Hamann, D. R. *Phys. Rev. B* **1985**, *31*, 805−813.
(49) Humphrey, W.; Dalke, A.; Schulten, K. J. *J. Mol. Graphics* **1996**, *14*, 33−38.